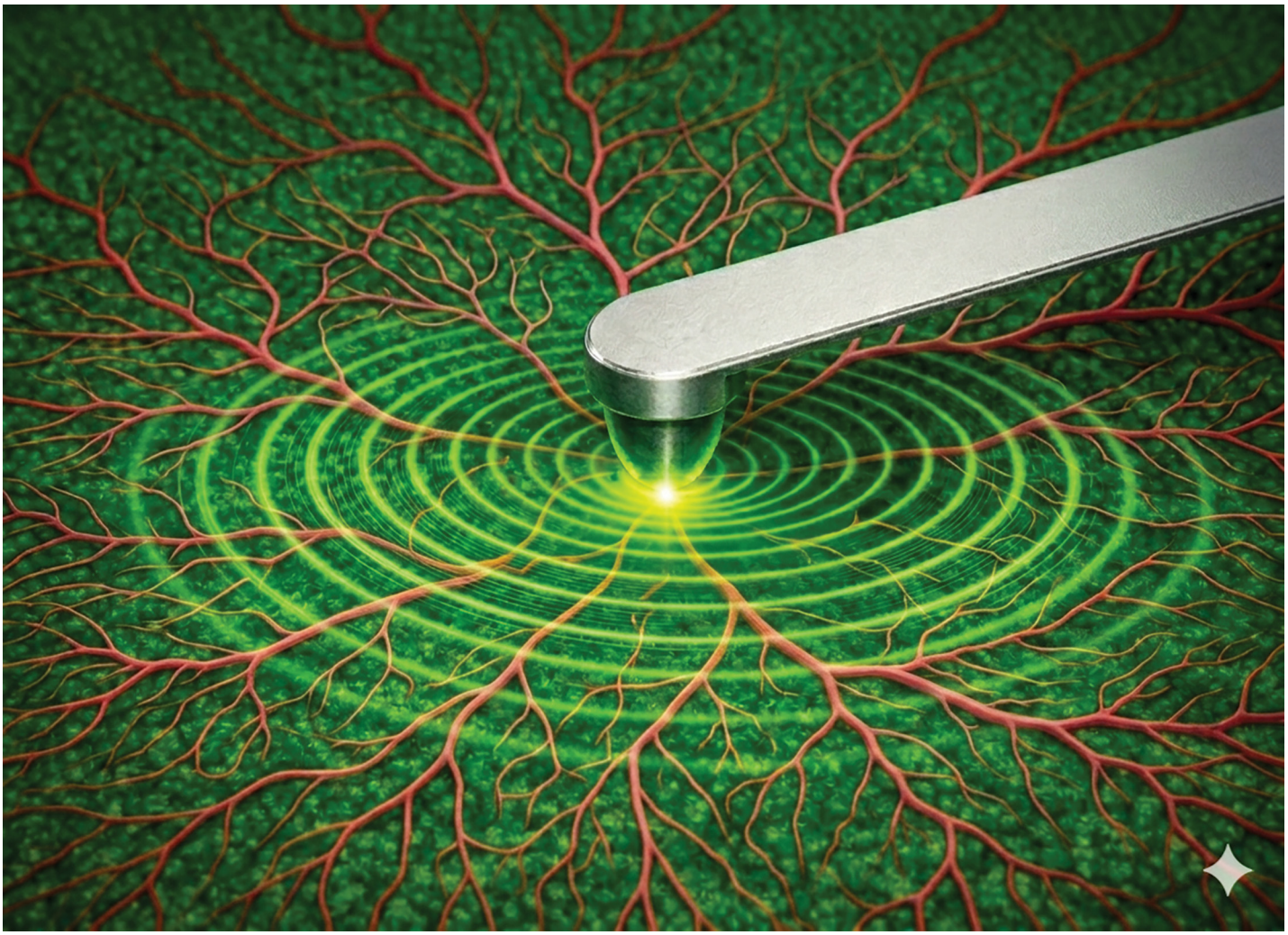

Showcasing research from Professor Sharon Gerecht's laboratory, Department of Biomedical Engineering, Duke University, Durham, North Carolina, USA.

Retina microrheology *via* oscillatory atomic force microscopy

The viscoelastic properties of tissues, specifically elasticity and viscosity, play a central role in development and disease progression. Conventional atomic force microscopy (AFM) indentation approaches, however, provide limited resolution of these complex mechanical behaviors. In this study, we implement oscillatory AFM-based microrheology to quantify both elastic and viscous contributions to tissue mechanics. Our results demonstrate that this approach more effectively characterizes mechanical behavior than standard indentation methods, enabling improved investigation of disease-associated changes and regenerative processes.

Image reproduced by permission of Connor Amelung from *Soft Matter*, 2026, **22**, 2629.
Cover image generated with AI.

As featured in:

See Sharon Gerecht *et al.*, *Soft Matter*, 2026, **22**, 2629.

ROYAL SOCIETY OF CHEMISTRY

rsc.li/soft-matter-journal

Registered charity number: 207890

Soft Matter

PAPER

View Article Online
View Journal | View Issue

Cite this: *Soft Matter*, 2026, **22**, 2629

Retina microrheology *via* oscillatory atomic force microscopy

Connor D Amelung, Colter E Oroke, Lucas Ramirez and Sharon Gerecht*

Viscoelastic properties of tissues, including elasticity and viscosity, are crucial for understanding development and disease progression. However, traditional atomic force microscopy (AFM) indentation methods provide limited insight into these complex tissue properties. This study establishes microrheology *via* oscillatory AFM to assess both the elastic and viscous components of tissue mechanics. We first compared indentation AFM to oscillatory AFM on mouse retinal tissue and found that the Young's modulus of indentation AFM (956.8 Pa) was statistically similar to the elastic component (storage modulus, E') of oscillatory AFM (920.2 Pa), while also providing the viscous component (loss modulus, E'' = 218.3 Pa), and the loss factor ($\tan(\delta)$ = 0.238) across a wide range of biologically relevant frequencies (1–100 Hz). We also found that optimization of input probe parameters, such as approach length, approach speed, applied force, and oscillation amplitude, is key for accurate measurements. To examine whether this approach can detect differences between healthy and diseased tissues, we applied it to murine retinas from healthy control mice and diabetic retinopathy mice, using the oxygen-induced retinopathy (OIR) mouse model. OIR retinas exhibited increased stiffness (E' = 3564.0 Pa) and a higher loss factor ($\tan(\delta)$ = 0.478) compared to healthy retinas (E' = 920.7, $\tan(\delta)$ = 0.263), suggesting changes in the extracellular matrix and highlighting how retinopathy may alter matrix properties. Finally, to assess the feasibility of using microrheology AFM on banked tissues biospecimens, we examined how tissue fixation affects the measurements. We found that formaldehyde fixation increased stiffness and elasticity, with OIR tissues consistently stiffer than WT tissues in both fixed and unfixed tissues, enabling valid cross-treatment comparisons. Our findings establish the benefits of microrheology in capturing tissue mechanical behavior, which is important for studying disease impact on tissue mechanics. This approach offers new insights into tissue viscoelasticity with implications for studying the dynamics of tissue mechanics in diseases and regeneration.

Received 20th October 2025,
Accepted 6th February 2026

DOI: 10.1039/d5sm01060h

rsc.li/soft-matter-journal

1. Introduction

Tissue mechanics are an important regulator of development, homeostasis, and disease. In healthy tissues, the dynamic interplay of mechanical signals regulates cell function, growth, and tissue remodeling.[1–3] Alterations in these tissue mechanics can disrupt these processes, contributing to the onset and progression of disease.[4–6] In particular, the viscoelastic properties of tissues are critical, as they determine how tissues respond to mechanical stress and strain.[1,7] This includes the balance between elastic and viscous components, where stress relaxation and the viscous behavior of tissues are key to understanding their response to mechanical forces.[8] For example, in diseases such as diabetic retinopathy, altered tissue mechanics can contribute to disease progression,[9,10] making it essential to study these properties in depth. However, current bulk rheological methods lack the granularity needed to fully capture the complexity of tissue mechanics, while techniques like atomic force microscopy (AFM) fall short in providing detailed viscous measurements, limiting their usefulness in viscoelastic applications.

AFM indentations measure the interaction forces between a probe and a sample surface, offering high spatial resolution and sensitivity to mechanical properties such as stiffness, elasticity, and damping.[11–13] While this technique has been successfully applied to various tissues to investigate changes in surface topography and mechanical stiffness associated with disease states,[14] indentations alone cannot quantify the complex, time-dependent mechanical properties inherently present in water-swollen tissues.

To address these limitations, microrheology has emerged as a promising approach, allowing for the study of local mechanical properties at the microscale. By employing oscillatory measurements of the AFM probe while in contact with the sample, microrheology measures the phase angle between stress and strain to quantify the relative contributions of elasticity and viscosity, providing a more detailed and nuanced understanding of tissue mechanical behavior. Early studies have utilized AFM to probe the viscoelastic properties of tissues, demonstrating the frequency dependency of hydrated matrices.[15,16] Additionally,

Department of Biomedical Engineering, Duke University, Durham, NC, 27708, USA. E-mail: sharon.gerecht@duke.edu

variations of AFM mapped the viscoelastic properties of cells,[17–21] protein condensates,[22] and cartilage and breast tissues,[23,24] but has not been utilized to compare viscoelastic profiles between disease states in tissues *via* multi-frequency oscillatory methodology.

While fresh tissues are generally ideal for rheological measurements, practical workflows often necessitate tissue fixation to preserve sample integrity over time. Fixation stabilizes tissues by halting enzymatic and structural changes, but it also introduces chemical and molecular alterations that can impact the tissue's mechanical properties. Existing literature comparing the effects of fixation on tissue mechanics is limited,[25,26] especially in relation to microrheology. In this study, we use microrheology AFM in both control and diabetic retinas, to explore how viscoelastic properties differ across varying retinal phenotypes and provide a tool to evaluate tissue mechanics. We provide a comprehensive comparison of tissue mechanics across different levels of fixation using both formaldehyde and methanol, offering new insights into how fixation procedures may alter tissue viscoelasticity and how these changes impact microrheological measurements. By integrating fixation studies with oscillatory AFM microrheology, we establish a reproducible framework for quantifying both elastic and viscous tissue mechanics in banked specimens, enabling rigorous cross-treatment and cross-phenotype comparisons. This advances biomechanical phenotyping beyond the constraints of fresh tissue analysis, opening new possibilities for leveraging archived clinical and research samples to investigate disease-related changes in tissue mechanics.

2. Experimental methods

2.1. Oxygen induced retinopathy mouse model

We followed a well-established OIR mouse model protocol. C57BL/6J (Jackson Laboratory) were used for the experiments.[27] In brief, mice were subjected to 75% oxygen from P7 to P12 (BioSpherix ProOx 360). On P12, mice were returned to room air. All studies were conducted under the Duke University Institutional Animal Care and Use Committee-approved animal protocol A070-22-04-25.

2.2. Retina fixation and flat mount

Eyes from P17 mice were enucleated and placed immediately in fixative solution or transport medium. For fixed tissues, eyes were submerged in 4% PFA or ice-cold methanol at timed durations of 5 or 30 minutes. For fresh tissues, eyes were submerged in PBS containing protease and phosphatase inhibitor cocktail (Thermo Fisher Scientific 78442) diluted to working concentration. The cornea, lens, and retina, were removed from the eye cup using dissection forceps and micro-scissors under a dissecting scope. Extracted retina tissues were adhered to positively charged glass slides (Fisherbrand 1255015) with the outer retina facing upward and submerged in 1× protease and phosphatase inhibitor (Thermo Fisher Scientific 78442) in PBS to prevent degradation.

2.3. Oscillatory atomic force microscopy

2.3.1. Cantilever alignment and calibration. Before each experiment, the AFM laser was aligned to the back of the cantilever using the Bruker Nanowizard V BioScience optical positioning system to maximize the photodiode sum signal. Alignment was adjusted in both X and Y until the signal reached the manufacturer-recommended range, and the position-sensitive photodetector was centered by adjusting detector offset controls until the vertical and horizontal difference signals were near zero in the free (non-contact) state. Optical lever sensitivity was confirmed during deflection sensitivity calibration on a clean glass substrate. Cantilever spring constants (0.15–0.21 N m^{-1} for SAA-SPH-1UM probes) were determined for each experiment using the built-in thermal tune method prior to sample measurements.

We used spherical AFM probes (SAA-SPH-1UM; nominal radius $R \approx 1$ μm), and accordingly applied a spherical Hertz contact model. Spherical probes are widely recommended for soft, hydrated tissues because they generate a larger, smoothly varying contact area that reduces localized stress concentrations and minimizes tip-induced nonlinearities.[28,29] Prior AFM analyses have shown that the inferred modulus is sensitive to indenter shape because contact-area evolution, and thus the force–indentation relationship, differs between spherical and sharp geometries.[30–34] In contrast, conical or pyramidal tips produce highly concentrated stresses and follow different scaling laws (*e.g.*, Sneddon-type), which can lead to higher apparent moduli and stronger depth dependence in soft biological materials.[28–30] For these reasons, a spherical geometry provides a more stable and physiologically appropriate contact for probing retinal tissue mechanics.

2.3.2. Measurement location and indentation regime. AFM measurements were performed while submerged using a Nanowizard V BioScience (Bruker) equipped with SAA-SPH-1UM probes (spring constant 0.15–0.21 N m^{-1}) with a setpoint of 3 nN, velocity of 2 μm s^{-1}, and retraction length of 4 μm. AFM measurements were performed in the mid-peripheral retina, approximately 25% of the retinal radius from the optic nerve head. With the outer retina facing upward and indentation depths of ~1 μm, the measurement primarily probes the outer retinal surface layers, including the photoreceptor outer segment–associated extracellular matrix (ECM) and adjacent outer limiting membrane region. Deeper layers (>10–20 μm beneath the surface) are not mechanically engaged at these indentation depths. Mid-peripheral sampling was chosen to avoid the mechanical heterogeneity near the optic nerve head and peripheral edge and was applied consistently across all specimens. A 25 × 25 μm scan area was defined, and 16 measurements were acquired within the region at room temperature on a vibration isolation table (TMC CleanBench).

2.3.3. Oscillatory measurement parameters and hydrodynamic considerations. The probe oscillated in a frequency shuffle of 1, 2.2, 4.5, 10, 22, 45, and 100 Hz for at least five cycles with an amplitude of 20 nm. Oscillatory measurements were conducted with the cantilever in steady contact with the tissue at the 3 nN setpoint, a regime in which the tip–sample interaction dominates the measured response. Given the small oscillation amplitude (20 nm) and the low-frequency range (1–100 Hz), the hydrodynamic drag on the cantilever in liquid is expected to contribute only a weak, slowly varying background relative to the contact force.[17,20,35] This background remains

well below the phase resolution of the measurement and does not measurably affect the extraction of $E'(\omega)$ or $E''(\omega)$. For this reason, and because a meaningful numerical decomposition of drag *versus* contact contributions cannot be obtained in this in-contact regime, no separate hydrodynamic correction was applied.

2.3.4. Contact mechanics framework and tip geometry. A spherical Hertzian contact model was used to convert the complex contact stiffness $K^*(\omega)$ to the complex Young's modulus $E^*(\omega)$. For an elastic half-space indented by a rigid sphere of radius R, the static contact relations are:

$$F = \frac{4}{3}E_r R^{1/2}\delta^{3/2}, a = \sqrt{R\,\delta},$$

where $E_r = E/(1-\nu^2)$ is the reduced modulus and a is the contact radius. Differentiation yields the small-signal contact stiffness

$$k = \frac{dF}{d\delta} = 2E_r a = \frac{2aE}{1-\nu^2}.$$

Extending this relation to the oscillatory (complex) domain gives:

$$K^*(\omega) = \frac{2aE^*(\omega)}{1-\nu^2},$$

and therefore

$$E^*(\omega) = \frac{(1-\nu^2)K^*(\omega)}{2a}.$$

In practice we evaluate the contact radius a at the static indentation depth δ_0 (*i.e.*, $a = \sqrt{R\delta_0}$) because our oscillation amplitude satisfies $\delta_1/\delta_0 \ll 1$ (see below).

SAA-SPH-1UM probes were used (manufacturer nominal spherical radius R_{nom} = 1 μm). We measured tip radius using the integrated imaging and report the measured radius R_{meas} = 0.981 ± 0.131 μm), as analyzed by ImageJ.

A Poisson's ratio of ν = 0.5 was used, consistent with the incompressible behavior of hydrated soft tissues such as retina;[36–38] the factor $(1-\nu^2)$ was therefore evaluated using this value.

Because $\delta_1/\delta_0 \approx 0.02$ (see below), contact-area changes during the sinusoidal oscillation are negligible; accordingly, a was taken from the static indentation δ_0 and treated as frequency-independent. If contact-area changes were non-negligible (large δ_1/δ_0), more advanced contact models accounting for dynamic contact radius would be required.

The Hertzian framework assumes a smoothly increasing contact area during indentation and is widely used for soft biological tissues. In our measurements, the static indentation depth was on the order of the nominal tip radius; under these conditions, the Hertz model provides an approximate mapping between contact stiffness and modulus, suitable for describing overall trends in the elastic and viscous response. All samples were measured using identical probes, setpoints, and oscillation amplitudes, ensuring consistent application of the model across conditions. We therefore interpret the extracted moduli as reflecting relative mechanical behavior under a common geometric framework.

2.3.5. Finite-thickness and adhesion considerations. Retinal tissue is approximately 150 μm thick at P17,[39] whereas the static indentation depth in our measurements was ~1 μm with a 20 nm oscillation amplitude. As the indentation depth was thus <1% of the sample thickness, the stress field remains fully contained within the tissue and does not interact with the underlying glass substrate. Under these conditions, finite-thickness or substrate corrections (*e.g.*, Dimitriadis-type models) are not required, as the assumptions of a semi-infinite elastic half-space are well satisfied for both indentation and oscillatory microrheology.

Approach–retract curves showed no significant adhesive pull-off under submerged conditions, indicating that adhesion does not materially affect modulus extraction.

2.3.6. Signal processing and extraction of viscoelastic parameters. Analysis of the generated force curves was conducted with a custom Python script, running off of the AFMforce library.[40] Forces and displacement data were converted into readable arrays. Prior to FFT analysis, force and indentation signals were smoothed using a symmetric Gaussian filter (window size: 3, radius: 150). The filter was applied in a forward–reverse (bidirectional) manner, resulting in a zero-phase operation that does not introduce temporal or phase lag.

To further confirm robustness, a sensitivity analysis was performed (Tables S1 and S2), evaluating $E'(\omega)$ and $E''(\omega)$ as a function of filter window size (3–5) and radius (50–200), compared to no filter. Across all window sizes, changes in E' were <5% and changes in E'' were <7%, demonstrating that modulus estimates were not sensitive to filter strength. We therefore conclude that the smoothing procedure does not distort phase or bias viscoelastic parameter estimation.

The contact point was calculated for force curves similar to methods used in NANOWIZARD5, and force curves were normalized to zero at that point.

The sinusoidal portion of the force and indentation signals was isolated and analyzed by Fast Fourier Transform (FFT). This yielded the oscillation amplitudes $F_1(\omega)$ and $\delta_1(\omega)$, as well as the phase difference $\Delta\phi(\omega)$ between the force and displacement. The complex contact stiffness was defined as:

$$K^*(\omega) = \frac{F_1(\omega)}{\delta_1(\omega)}e^{i\Delta\varphi(\omega)}.$$

A spherical indenter geometry was assumed for the SAA-SPH-1UM probes (nominal radius R = 1 μm). Under Hertzian contact, the complex contact stiffness relates to the complex modulus through:

$$K^*(\omega) = 2aE^*(\omega),$$

where the contact radius is

$$a = \sqrt{R\,\delta_0},$$

and δ_0 is the static indentation depth at the 3 nN setpoint (approximately 1 μm across samples). The complex modulus was therefore computed as:[20,35]

$$E^*(\omega) = \frac{K^*(\omega)}{2a}.$$

The storage modulus E' corresponds to the in-phase (elastic) component of E^*, the loss modulus E'' corresponds to the out-of-phase (viscous) component, and the loss factor was calculated as $\tan(\delta) = E''/E'$.

Unless otherwise noted, oscillatory measurements used an amplitude of δ_1 = 20 nm, giving a small-signal ratio $\delta_1/\delta_0 \approx 0.02$, confirming linear viscoelastic probing. Only curves with well-resolved sinusoidal oscillations were retained, requiring FFT-derived sinusoidal fits with $R^2 > 0.8$ and an oscillatory force signal-to-noise ratio (SNR) ≥ 10. Additional filtering based on storage modulus thresholds (maximum of 40 kPa), loss tangent limits (minimum 0, maximum 8), and frequency-wise Z-score outlier detection (Z-score = 3) was applied as described above. Curve data was then packaged into a tab-separated variable file for later statistical analysis.

2.4. Statistics

Details of replicates for each experiment can be found in the figure legends. All bar graphs represent means ± SD unless otherwise denoted. The authors performed statistical analysis using GraphPad Prism 10 (GraphPad Software Inc.). This software was also used to perform t-tests and one-way ANOVA with multiple comparisons to determine significance. Significance levels were set at * $p < 0.05$, ** $p < 0.01$, *** $p < 0.001$, and **** $p < 0.0001$.

3. Results and discussion

3.1. Oscillation provides additional mechanical context over traditional indentation AFM

Traditionally, AFM force spectroscopy measures mechanical properties like stiffness through contact mode, where the AFM tip is brought into direct contact with the sample. This technique provides precise measurements of surface roughness and topography at the nanoscale, making it ideal for characterizing hard and rigid materials. However, it provides limited information about the viscoelastic properties of a sample, as it is mainly focused on topography and basic force measurements, making it less suitable for studying complex, soft materials or biological samples where the viscoelastic behavior is crucial. Oscillatory AFM, specifically used for microrheology, involves oscillating the AFM tip at a defined frequency over the sample, which allows for the measurement of both the elastic component (storage modulus, E') and the viscous component (loss modulus, E'') of the material. This method is particularly valuable for studying soft materials, biological tissues, or polymers, as it provides insights into their viscoelastic properties without causing significant damage to the sample. By analyzing the phase shift and amplitude of the oscillations, oscillatory AFM can provide detailed information about the material's response to mechanical stress, making it highly effective for microrheological measurements.

The spatial resolution of oscillatory AFM microrheology is set primarily by the lateral extent of the indentation footprint and the spacing between measurement points. With a spherical probe of ~1 μm radius, the contact radius is on the order of 0.5–1 μm, enabling sampling of mechanical properties at approximately micron-scale lateral resolution. In practice, our measurements were acquired on a 25 × 25 μm region using a 4 × 4 grid (16 points), demonstrating that the technique can probe local mechanical heterogeneity at cellular to subcellular length scales. This spatial resolution is not achievable with bulk rheology or indentation methods requiring larger footprints, underscoring AFM's suitability for microscale tissue characterization.

First, we aimed to directly compare measurements of murine retinal tissues taken *via* traditional indentation to those obtained by oscillatory microrheology. Following extraction, retinas were placed on positively charged glass slides to allow adhesion. Once adhered, the retinas were placed on the AFM stage and submerged in PBS containing protease inhibitors to prevent protein degradation and preserve mechanical properties (Fig. 1A and B). Submersion is also necessary for microrheology, as many commercially available cantilevers perform optimally with increased resistance from water submersion. Both indentation and microrheology were performed on the same sample using the same cantilever (Fig. 1C and D). Indentation measurements revealed that control mice had

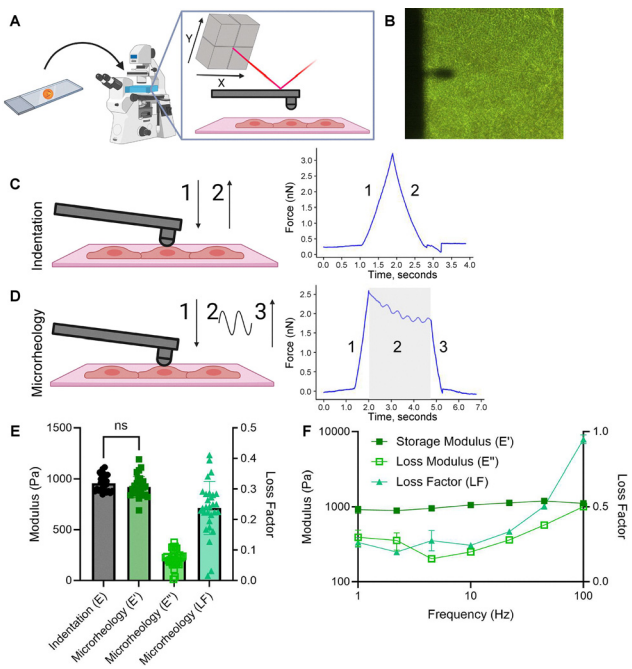

Fig. 1 AFM Indentation and Microrheology Measurements on Retinas. (A) Retinas were placed on slides and analyzed on the AFM. (B) Images of the retina when placed on AFM stage. The AFM unit is combined with brightfield microscopy to enable manual selection of measurement regions based. (C) Schematic of cantilever movement in indentation AFM. The cantilever enters the tissue and immediately retracts upon reaching the specified normal force. (D) Schematic of cantilever movement in microrheology AFM. Once reaching the desired normal force, the cantilever oscillates at a known frequency and amplitude to measure the time-dependent behavior within the sample. (E) AFM performed on control samples *via* indentation (Young's Modulus, E) and microrheology (storage modulus [E'], loss modulus [E''], and loss factor). N = 25–29 measurements collected across 3 retina. (F) Microrheology sweep of storage modulus between 1-100 Hertz, with error bars denoting SEM. N = 33–63 measurements at each timepoint collected across 3 retina.

an average Young's Modulus (E) of 956 Pa (Fig. 1E). Microrheology results showed similar trends, with an average storage modulus (E') of 920 Pa (Fig. 1E). While there was no significant difference, we expected the downward trend as the complex modulus is broken into constituent components. In addition to measuring the elastic component (E'), oscillatory measurements allowed comparison of the viscous component (E'') and the loss factor ($\tan\delta$), defined as E''/E'. We further performed these measurements across a wide range of frequencies (Fig. 1F), and found that all components increased with frequency. This frequency-dependent increase in modulus likely arises from the viscoelastic relaxation dynamics of the retinal ECM, where applied deformations at higher frequencies outpace the characteristic relaxation times of the collagen- and proteoglycan-rich network.[41,42] Under these conditions, fluid redistribution and molecular rearrangements are kinetically suppressed, forcing the load to be supported predominantly by the elastic fiber network and resulting in higher apparent stiffness.[43,44]

Thus, microrheology using oscillatory AFM offers a more detailed analysis of the mechanical properties of the retina by measuring both the elastic and viscous components of the ECM. Unlike traditional indentation, which only captures the elastic response, microrheology allows for the assessment of the material's frequency-dependent behavior, providing insights into the viscoelastic nature of the tissue. This comprehensive approach is particularly valuable for studying complex biological materials like the retina, where changes in both elasticity and viscosity play critical roles in tissue function and pathology.

3.2. AFM input parameters require optimization based on sample type

In optimizing the measurement conditions, we observed that the results were highly sensitive to the AFM input parameters, such as cantilever movement, oscillation frequency, and force applied. These systems offer the flexibility of custom movement of the cantilever relative to the sample, allowing for precise control over the interaction between the tip and the material being measured. However, this customization also necessitates careful optimization to ensure that the measurements reflect the true elastic properties of the sample without introducing viscoelastic deformation.[14,45] If the cantilever moves too quickly or with excessive force, it can induce strain on the sample, distorting the measurement, particularly in soft materials where viscoelastic effects are more pronounced. To avoid this, parameters such as oscillation amplitude and frequency must be fine-tuned to achieve an optimal balance between capturing the elastic response and preventing significant deformation of the sample. Moreover, variations in sample properties, such as roughness or heterogeneity, may require adjustments to these parameters for accurate results. Thus, optimizing AFM input parameters is crucial to obtaining reliable and reproducible data, particularly when measuring the mechanical properties of complex, viscoelastic materials.

The approach length refers to the resting distance between the cantilever and the sample before measurement. Approach length tested in the parameter sweep ranged from 1–10 μm, with the standard experimental length set to 4 μm. We observed that shorter approach lengths, where the cantilever remains closer to the sample, resulted in stiffer readings (Fig. 2A). This suggests that shorter approach lengths may not provide enough distance for some samples, especially those with high adherence forces or rough surface topography, to fully unadhere or prevent sample shifting. This can lead to compression and artifacts in the measurements. The approach speed, or the velocity at which the cantilever approaches the sample, was also taken into consideration. Approach speed ranged from 1–10 μm s^{-1}, with the standard experimental speed set to 2 μm s^{-1}. We found that E' decreased with increasing approach speed (Fig. 2B), likely due to less accurate detection of the true contact point at rapid approach, which leads to a slight underestimation of indentation depth and therefore a lower extracted modulus in the Hertz fit. Additionally, applied force, or the amount of force the cantilever exerts on the sample before measurements, was found to increase E' due to greater indentation depths (Fig. 2C), leading to more tissue contact and higher resistance, varied from 1–10 nN with 3 nN as a standard force. Lastly, we examined oscillation amplitude, which refers to the magnitude of displacement between the highest and lowest oscillation positions. We varied the amplitude from 2–50 nm, utilizing 20 nm as the experimental standard. We found that lower amplitudes resulted in both higher E' values and significantly greater standard

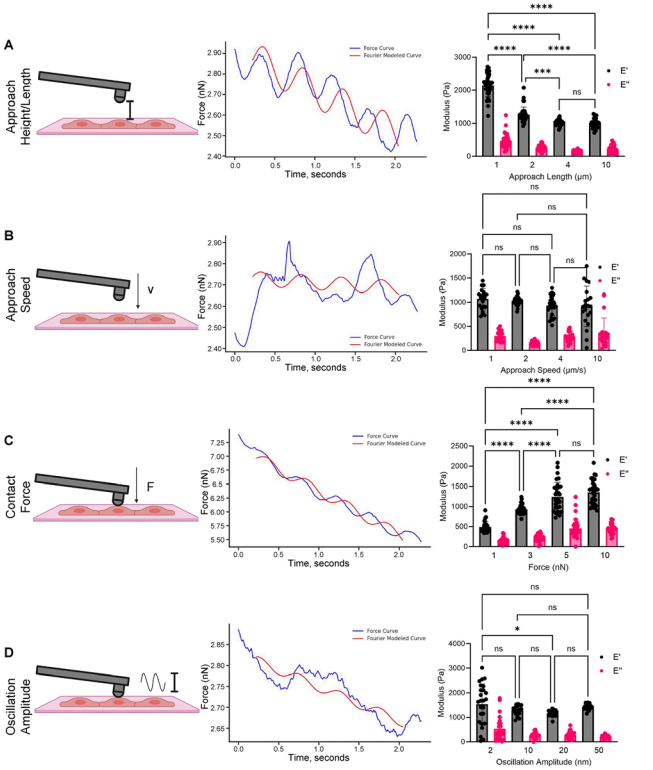

Fig. 2 Impact of microrheology input parameters on measurements. Varying the input parameters of approach length (A), approach speed (B), applied force (C), and oscillation amplitude (D) are key to accurately characterizing sample tissues. Sample curves demonstrate the impact of incorrect parameter selection on curve geometry, leading to unrepresentative measurements. N = 18–36 measurements collected across three retina. Significance levels were set at * $p \leq 0.05$, ** $p \leq 0.01$, *** $p \leq 0.001$, **** $p \leq 0.0001$.

deviation of E' (Fig. 2D), indicating that insufficient amplitude may fail to create a strong enough signal-to-noise ratio, allowing tissue shifts and other sources of error to influence the results.

Overall, optimizing input parameters, such as approach length, speed, applied force, and oscillation amplitude, is crucial for obtaining accurate and reliable measurements in AFM experiments. Proper parameter selection minimizes artifacts caused by sample shifts, stress-relaxation issues, and noise, ensuring precise characterization of the material's mechanical properties.

3.3. Microrheology quantifies increased stiffness and elasticity in diabetic retinas

We next aimed to utilize microrheology to compare the impact of retinal disease on mechanical properties. We used retinas from mice with oxygen-induced retinopathy (OIR), a model for studying diabetic retinopathy.[46,47] OIR mice are valuable for investigating retinal vascular dysfunction, endothelial instability, and abnormal angiogenesis, as well as for testing potential therapies. Previous studies in OIR mice have shown significantly reduced vascular stability and abnormal ECM deposition.[48–50] Based on these observations, we hypothesized that OIR retinas would exhibit altered viscoelastic properties compared to control retinas.

In OIR, neonatal mice are exposed to high oxygen levels, leading to abnormal blood vessel development. When returned to normal oxygen levels, retinal ischemia and neovascularization occur, mirroring the vascular changes seen in diabetic retinopathy (Fig. 3A).[9,51,52] Microrheology measurements revealed that OIR retinas had increased stiffness compared to control mice, with stiffness increasing from 920 Pa to 3563 Pa (Fig. 3B). In addition to the increased elastic component (E'), oscillatory measurements allowed comparison of the viscous component (E'') and the loss factor, the ratio between the elastic and viscous components. We found that the viscous components were similar, but OIR retinas exhibited a more viscous loss factor, suggesting an increase in ECM dissipation behaviour. These comparisons were consistent across a wide range of frequencies (Fig. 3C–E), and found that all components increased with frequency. This frequency-dependent behaviour is likely caused by the increased rigidity of the ECM in OIR retinas.

In summary, oscillatory AFM revealed that OIR retinas exhibit increased stiffness compared to control retinas. The use of oscillatory AFM allowed us to probe not only the elastic component of the matrix but also the viscous properties, offering a comprehensive understanding of the ECM's mechanical behavior. The oscillatory measurements highlighted an increase in the loss factor in OIR retinas, suggesting increase ECM dissipation behaviour, which may contribute to the altered vascular and cellular behaviour observed in diabetic retinopathy. This approach highlights the value of oscillatory AFM in studying dynamic mechanical properties, as it offers deeper insights into the viscoelastic nature of the ECM and its role in tissue remodeling and dysfunction.

3.4. Formaldehyde and methanol fixation increase retina tissue stiffness and elasticity

Lastly, we aimed to explore the impact of fixation on microrheology measurements. AFM force spectroscopy measurements

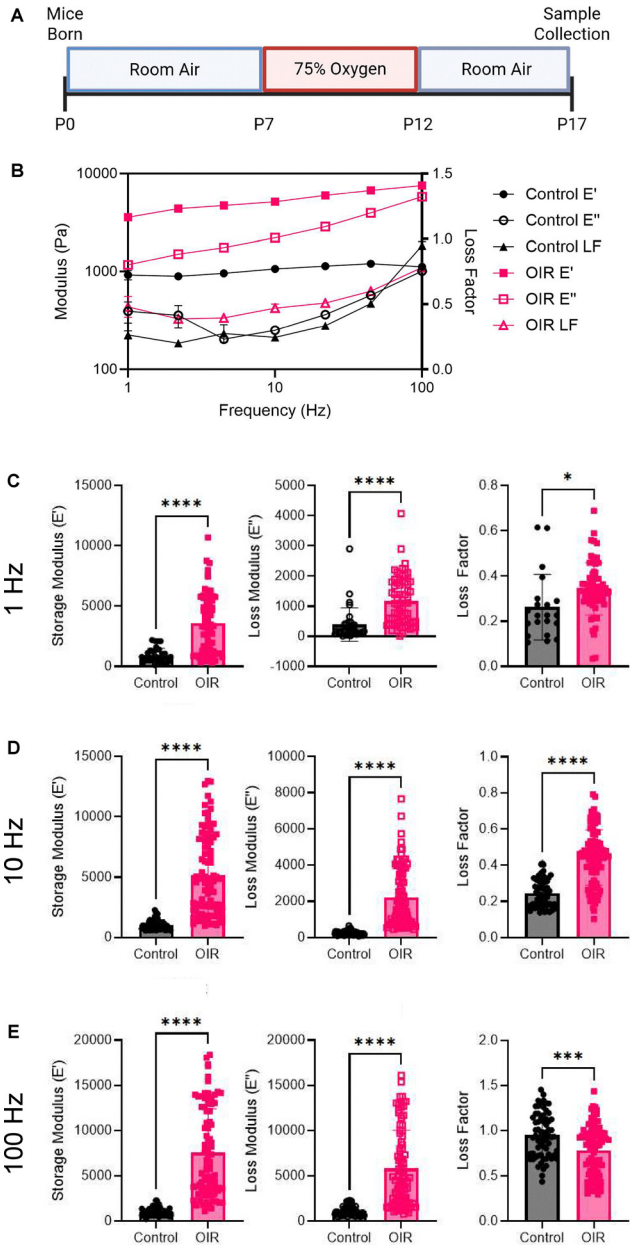

Fig. 3 Microrheology measurements across control and OIR mice. Experimental timeline from mouse birth to sacrifice, with retinas measured *via* AFM on postnatal day 17 (P17) (A). Frequency sweep of control and diabetic mice across 1–100 Hertz (B), with error bars representing SEM. Comparisons were similar across the range of frequencies (C)–(E). N = 21–98 measurements collected across three retina. Significance levels were set at * $p \leq 0.05$, ** $p \leq 0.01$, *** $p \leq 0.001$, **** $p \leq 0.0001$.

are often carried out on fixed human patient samples, as these specimens are typically difficult to obtain in fresh form and are more commonly accessible through biobanked collections.[53] Using fixed samples not only overcomes the logistical challenges associated with sample availability but also enables extensive and prolonged research, including detailed mechanobiological analyses that can be revisited over time without compromising sample integrity.[54] Fixation preserves the tissue's structural integrity and prevents degradation, making it easier

to handle and prepare for analysis. A common fixation method is using formaldehyde, which crosslinks proteins and stabilizes tissue structure (Fig. 4A). Fixation using methanol, which rapidly dehydrates and condensates samples, is also utilized in research settings (Fig. 4D). However, it is important to note that fixation can alter the mechanical properties of the tissue, which may influence the interpretation of AFM data. While the response to fixation is understood for traditional AFM,[25,26] the impact of fixation on viscoelastic measurements is unknown.

To characterize microrheology measurements following fixation, we fixed control and OIR retinas in both formaldehyde and methanol for 5 or 30 minutes to examine how fixation time influences mechanical properties. Microrheology sweeps revealed that formaldehyde fixation time was consistently associated with increased stiffness across all frequencies (Fig. 4B), while exhibiting a substantial increase in elasticity (Fig. 4C), representative of the increased degree of crosslinking. Notably, while control and OIR samples both increased proportionally in stiffness, loss factor measurements were less consistent. It is probable that the variable protein deposition and architecture lead to more predictable trends in stiffnesses in response to fixation, but are less predictable with loss factor due to differential crosslinking based on protein composition. Methanol preservation, however, led to more variable results across both stiffness (Fig. 4E) and loss factor (Fig. 4F). We attribute this unpredictability to the nature of protein condensation, being that protein aggregates form unstable, heterogeneous clusters that lead to variability in mechanical analysis.

Fixation substantially altered the absolute values of the storage and loss moduli, as expected from chemical crosslinking, as seen with formaldehyde, or protein condensation, as seen with methanol. Nonetheless, in fully fixed samples, such as those treated for 30 minutes, differences between control and OIR retinas were still detectable, indicating that fixation preserves certain relative mechanical contrasts even though it shifts absolute modulus values. In contrast, very short fixation, as seen in the 5 minute group, did not consistently maintain this separation, likely due to incomplete or heterogeneous crosslinking.

These findings suggest that when a uniform and complete fixation protocol is applied, mechanically meaningful distinctions between disease states can still be resolved, even though fixed tissues cannot recapitulate the absolute mechanics of fresh samples. This supports the feasibility of using appropriately fixed or biobanked specimens for comparative micromechanical analyses, particularly in translational settings where fresh tissue is not available.

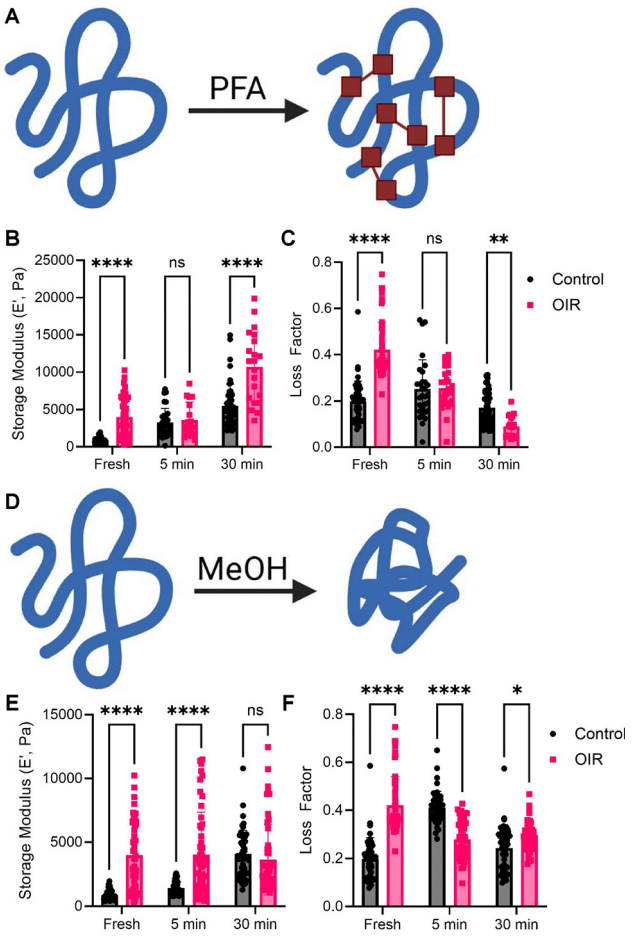

Fig. 4 Influence of formaldehyde and methanol fixation on control and OIR retinas. (A) Paraformaldehyde fixes by crosslinking exposed lysine. (B) Storage modulus of PFA fixed samples. (C) Loss factor of PFA fixed samples. (D) Methanol preserves by dehydrating and condensing proteins. (E) Storage modulus of MeOH fixed samples. (F) Loss factor of MeOH fixed samples. N = 28–87 measurements collected across three retina. Significance levels were set at * $p \leq 0.05$, ** $p \leq 0.01$, *** $p \leq 0.001$, **** $p \leq 0.0001$.

4. Conclusions

This study highlights the power of oscillatory AFM-based microrheology in assessing the viscoelastic properties of retinal tissue and its changes in disease states, such as diabetic retinopathy. Through comparisons between traditional indentation and oscillatory microrheology, we demonstrated the importance of measuring both elastic and viscous components of the tissue to capture a more comprehensive view of its mechanical behavior. The results from OIR mice, a model for retinal vascular dysfunction, showed increased tissue stiffness and a more viscous loss factor, suggesting ECM dissipation behaviour, which may contribute to the altered tissue behaviour seen in retinal diseases. Importantly, these findings underscore the utility of microrheology in detecting subtle changes in tissue mechanics that would be missed by conventional techniques.

Furthermore, we explored the effects of tissue fixation on microrheological measurements, revealing that fixation procedures, especially formaldehyde, increase tissue stiffness and elasticity, likely due to crosslinking and other chemical changes. While fixation may alter mechanical properties, our results show that relative comparisons between control and OIR tissues were preserved when fully fixed with formaldehyde, indicating that such measurements remain valid as long as samples are treated similarly. This provides a foundation for utilizing fixed

tissues in microrheology-based studies, particularly when experimental constraints require the use of fixed samples.

Regarding future directions, further investigation into the long-term stability of fixed tissue samples, as well as optimization of AFM parameters for different tissue types, will be essential for refining this technique. Additionally, exploring the molecular mechanisms behind the observed changes in tissue mechanics in diabetic retinopathy could reveal potential therapeutic targets for improving retinal health. Microrheology-based AFM presents a powerful tool for advancing our understanding of tissue mechanics in health, disease, and aging tissue, offering promising insights for both diagnostic and therapeutic applications.

Author contributions

CDA: writing original draft, investigation, data curation, formal analysis, visualization, writing – review & editing. CEO: investigation, resources, writing – review & editing. LR: resources, writing – review & editing. SG: conceptualization, methodology, validation, supervision, project administration, writing – review & editing, funding acquisition.

Conflicts of interest

There are no conflicts to declare.

Data availability

The data underpinning this article is deposited in the Duke University Libraries' Research Data Repository and made publicly accessible *via* a persistent DOI: https://doi.org/10.7924/r4qv3sz88.

Supplementary information (SI) is available. See DOI: https://doi.org/10.1039/d5sm01060h.

Acknowledgements

We acknowledge support from Duke Science and Technology. CDA is supported by the National Science Foundation GRFP GDS 2139754. BioRender was utilized to generate figure schematics.

References

1 Z. Wei, R. Schnellmann, H. C. Pruitt and S. Gerecht, *Cell Stem Cell*, 2020, **27**, 798–812.
2 Y. Yu, Y. Leng, X. Song, J. Mu, L. Ma, L. Yin, Y. Zheng, Y. Lu, Y. Li, X. Qiu, H. Zhu, J. Li and D. Wang, *Arterioscler., Thromb., Vasc. Biol.*, 2023, **43**, 1887–1899.
3 M. Urbanczyk, S. L. Layland and K. Schenke-Layland, *Matrix Biol.*, 2020, **85–86**, 1–14.
4 S. Safaei, R. Sajed, A. Shariftabrizi, S. Dorafshan, L. Saeednejad Zanjani, M. Dehghan Manshadi, Z. Madjd and R. Ghods, *Cancer Cell Int.*, 2023, **23**, 143.
5 A. Heinz, *Ageing Res. Rev.*, 2021, **66**, 101255.
6 V. Gkretsi and T. Stylianopoulos, *Front. Oncol.*, 2018, **8**, DOI: 10.3389/fonc.2018.00145.
7 M. C. Lampi and C. A. Reinhart-King, *Sci. Trans. Med.*, 2018, **10**, eaao0475.
8 N. E. Friend, A. J. McCoy, J. P. Stegemann and A. J. Putnam, *Biomaterials*, 2023, **295**, 122050.
9 M. Vähätupa, T. A. H. Järvinen and H. Uusitalo-Järvinen, *Front. Pharmacol.*, 2020, **11**, DOI: 10.3389/fphar.2020.00873.
10 M. Vähätupa, J. Nättinen, A. Jylhä, U. Aapola, M. Kataja, P. Kööbi, T. A. H. Järvinen, H. Uusitalo and H. Uusitalo-Järvinen, *Invest Ophthalmol. Visual Sci.*, 2018, **59**, 3294–3306.
11 A. Calò, Y. Romin, R. Srouji, C. P. Zambirinis, N. Fan, A. Santella, E. Feng, S. Fujisawa, M. Turkekul, S. Huang, A. L. Simpson, M. D'Angelica, W. R. Jarnagin and K. Manova-Todorova, *Sci. Rep.*, 2020, **10**, 15664.
12 P. K. Viji Babu and M. Radmacher, *Front. Neurosci.*, 2019, **13**, DOI: 10.3389/fnins.2019.00600.
13 D. H. Cho, S. Aguayo and A. X. Cartagena-Rivera, *Biomaterials*, 2023, **303**, 122389.
14 Y. Shen, T. Schmidt and A. Diz-Muñoz, *STAR Protoc.*, 2020, **1**, 100167.
15 H. T. Nia, I. S. Bozchalooi, Y. Li, L. Han, H.-H. Hung, E. Frank, K. Youcef-Toumi, C. Ortiz and A. Grodzinsky, *Biophys. J.*, 2013, **104**, 1529–1537.
16 R. Oftadeh, J. Heilig, F. Zaucke, A. Niehoff and A. J. Grodzinsky, *Osteoarthritis Cartilage*, 2018, **26**, S61–S62.
17 R. Takahashi and T. Okajima, *Appl. Phys. Lett.*, 2015, **107**, 173702.
18 Y. M. Efremov, T. Okajima and A. Raman, *Soft Matter*, 2020, **16**, 64–81.
19 P. Nietmann, J. E. F. Bodenschatz, A. M. Cordes, J. Gottwald, H. Rother-Nöding, T. Ostwald and A. Janshoff, *Biophys. J.*, 2022, **121**, 361–373.
20 P. D. Garcia, C. R. Guerrero and R. Garcia, *Nanoscale*, 2020, **12**, 9133–9143.
21 B. Yan, J. Ren, X. Zheng, Y. Liu and Q. Zou, *Biomech. Model. Mechanobiol.*, 2017, **16**, 1857–1868.
22 X. Li, J. van der Gucht, P. Erni and R. de Vries, *J. Colloid Interface Sci.*, 2023, **632**, 357–366.
23 M. Tschaikowsky, T. Neumann, S. Brander, H. Haschke, B. Rolauffs, B. N. Balzer and T. Hugel, *Acta Biomater.*, 2021, **126**, 315–325.
24 G. Fabris, A. Lucantonio, N. Hampe, E. Noetzel, B. Hoffmann, A. DeSimone and R. Merkel, *Biophys. J.*, 2018, **115**, 1770–1782.
25 M. Iwashita, T. Nomura, T. Suetsugu, F. Matsuzaki, S. Kojima and Y. Kosodo, *Front. Cell Dev. Biol.*, 2020, **8**, 574619.
26 S.-O. Kim, J. Kim, T. Okajima and N.-J. Cho, *Nano Converg.*, 2017, **4**, 5.
27 H. Cho, B. L. Macklin, Y.-Y. Lin, L. Zhou, M. J. Lai, G. Lee, S. Gerecht and E. J. Duh, *JCI Insight*, 1828, **5**, e13.
28 Q. D. Nguyen and K.-H. Chung, *Ultramicroscopy*, 2019, **202**, 1–9.
29 E. Kim, A. L. Ramos Figueroa, M. Schrock, E. Zhang, C. J. Newcomb, Z. Bao and L. Michalek, *STAR Protoc.*, 2025, **6**, 103809.
30 S. V. Kontomaris, A. Malamou, G. M. Ismail, I. Psychogios and A. Stylianou, *Next Mater.*, 2025, **9**, 101299.
31 D. Sicard, L. E. Fredenburgh and D. J. Tschumperlin, *J. Mech. Behav. Biomed. Mater.*, 2017, **74**, 118–127.

32 T. Igarashi, S. Fujinami, T. Nishi, N. Asao and K. Nakajima, *Macromolecules*, 2013, **46**, 1916–1922.
33 K. Nakajima, M. Ito, D. Wang, H. Liu, H. K. Nguyen, X. Liang, A. Kumagai and S. Fujinami, *Microscopy*, 2014, **63**, 193–208.
34 Z. Al-Rekabi and S. Contera, *Proc. Natl. Acad. Sci. U. S. A.*, 2018, **115**, 2658–2663.
35 Y. M. Efremov, T. Okajima and A. Raman, *Soft Matter*, 2019, **16**, 64–81.
36 J. F. Koretz and G. H. Handelman, *Vision Res.*, 1983, **23**, 1679–1686.
37 E. A. Hermans, P. J. W. Pouwels, M. Dubbelman, J. P. A. Kuijer, R. G. L. van der Heijde and R. M. Heethaar, *Invest. Ophthalmol. Vis. Sci.*, 2009, **50**, 281–289.
38 K. Wang and B. K. Pierscionek, *Prog. Retinal Eye Res.*, 2019, **71**, 114–131.
39 L. R. Ferguson, J. M. D. Ii, S. Balaiya, S. Grover and K. V. Chalam, *PLoS One*, 2013, **8**, e67265.
40 T. Haraszti, AFM Force Python Package, 2025, https://github.com/tomio13/AFMforce.
41 E. M. Carvalho and S. Kumar, *Acta Biomater.*, 2023, **163**, 146–157.
42 B. Wu, P. Pu, S. Zhao, I. Izadikhah, H. Shi, M. Liu, R. Lu, B. Yan, S. Ma and B. Markert, *PLoS One*, 2020, **15**, e0235822.
43 E. Tanaka, J. Aoyama, M. Tanaka, T. Van Eijden, M. Sugiyama, K. Hanaoka, M. Watanabe and K. Tanne, *J. Biomed. Mater. Res. A*, 2003, **65**, 386–392.
44 D. Huang, Y. Huang, Y. Xiao, X. Yang, H. Lin, G. Feng, X. Zhu and X. Zhang, *Acta Biomater.*, 2019, **97**, 74–92.
45 M. J. Rosenbluth, W. A. Lam and D. A. Fletcher, *Biophys. J.*, 2006, **90**, 2994–3003.
46 L. E. Smith, E. Wesolowski, A. McLellan, S. K. Kostyk, R. D'Amato, R. Sullivan and P. A. D'Amore, *Invest. Ophthalmol. Vis. Sci.*, 1994, **35**, 101–111.
47 E. Kermorvant-Duchemin, P. Sapieha, M. Sirinyan, M. Beauchamp, D. Checchin, P. Hardy, F. Sennlaub, P. Lachapelle and S. Chemtob, *Doc. Ophthalmol.*, 2010, **120**, 51–60.
48 S. Li Calzi, L. C. Shaw, L. Moldovan, W. C. Shelley, X. Qi, L. Racette, J. L. Quigley, S. D. Fortmann, M. E. Boulton, M. C. Yoder and M. B. Grant, *JCI Insight*, **4**, e129224.
49 T. Maretzky, C. P. Blobel and V. Guaiquil, *Invest. Ophthalmol. Vis. Sci.*, 2014, **55**, 6774–6782.
50 B. Aguirre, M.-C. Lin, E. Araujo, C.-H. Lu, D. Casero, M. Sun, S. Nusinowitz, J. Hanson, K. Calkins, L. Gordon, M. Wadehra and A. Chu, *Invest. Ophthalmol. Vis. Sci.*, 2024, **65**, 10.
51 A. S. Dayoub, E. Acharya, A. Dibas, H. P. Jones and S. Acharya, *Cells*, 2024, **13**, 1371.
52 J. Woods and S. Biswas, *Mol. Cell. Pediatr.*, 2023, **10**, 12.
53 G. Mirizzi, F. Jelke, M. Pilot, K. Klein, G. G. Klamminger, J.-J. Gérardy, M. Theodoropoulou, L. Mombaerts, A. Husch, M. Mittelbronn, F. Hertel and F. B. Kleine Borgmann, *Molecules*, 2024, **29**, 1167.
54 L. w Francis, D. Gonzalez, T. Ryder, K. Baer, M. Rees, J. o White, R. s Conlan and C. j Wright, *J. Microscopy*, 2010, **240**, 111–121.